

Globular pattern formation of hierarchical ceria nanoarchitecture

Noboru Aoyagi (✉ aoyagi.noboru@jaea.go.jp)

Japan Atomic Energy Agency (JAEA) <https://orcid.org/0000-0002-0913-2742>

Ryuhei Motokawa

Japan Atomic Energy Agency

Masahiko Okumura

Japan Atomic Energy Agency

Takumi Saito

The University of Tokyo <https://orcid.org/0000-0002-4403-9607>

Shotaro Nishitsuji

Department of Organic Materials Science, Graduate School of Organic Materials Science, Yamagata University

Tomitsugu Taguchi

National Institutes for Quantum and Radiological Science and Technology

Takumi Yomogida

Japan Atomic Energy Agency (JAEA)

Atsushi Ikeda-Ohno

Japan Atomic Energy Agency (JAEA)

Article

Keywords: sissipative structures, hierarchical ceria nanoarchitecture, nanoparticles

Posted Date: June 22nd, 2021

DOI: <https://doi.org/10.21203/rs.3.rs-604840/v1>

License:   This work is licensed under a Creative Commons Attribution 4.0 International License.

[Read Full License](#)

1
2
3
4
5
6
7
8
9
10
11
12
13
14
15
16
17
18
19
20
21
22
23

Globular pattern formation of hierarchical ceria nanoarchitecture

Noboru Aoyagi^{1*}, Ryuhei Motokawa², Masahiko Okumura³, Takumi Saito^{1,4},
Shotaro Nishitsuji⁵, Tomitsugu Taguchi⁶, Takumi Yomogida⁷ and Atsushi Ikeda-Ohno¹

¹Advanced Science Research Centre (ASRC), Japan Atomic Energy Agency (JAEA), Tokai-mura, Ibaraki 319-1195 Japan

²Materials Sciences Research Centre (MSRC), Japan Atomic Energy Agency (JAEA), Tokai-mura, Ibaraki 319-1195 Japan

³Centre for Computational Science and e-Systems, JAEA, Kashiwa, Chiba 277-0871, Japan

⁴Nuclear Professional School, School of Engineering, The University of Tokyo, Ibaraki 319-1188 Japan

⁵Graduate School of Science and Engineering, Yamagata University, Yonezawa, Yamagata 992-8510, Japan

⁶National Institutes for Quantum and Radiological Science and Technology, Tokai-mura, Ibaraki 319-1106, Japan

⁷Nuclear Science and Engineering Centre (NSEC), Japan Atomic Energy Agency (JAEA), Tokai-mura, Ibaraki 319-1195 Japan

Author Note

*E-mail: aoyagi.noboru@jaea.go.jp

Abstract

26
27
28
29
30
31
32
33
34
35
36
37
38
39
40
41
42
43
44
45
46

Dissipative structures often appear as an unstable counterpart of ordered structures owing to fluctuations that do not form a homogeneous phase. Even a multiphase mixture may simultaneously undergo one chemical reaction near equilibrium and another one that is far from equilibrium. Here, we observed in real time crystal seed formation and simultaneous nanocrystal aggregation proceeding from Ce^{IV} complexes to CeO_2 nanoparticles in an acidic aqueous solution, and investigated the resultant hierarchical nanoarchitecture. The formed particles exhibited two very different size ranges. The hierarchically assembled structures in solutions were CeO_2 colloids, viz. primary core clusters (1–3 nm) of crystalline ceria and secondary clusters (20–30 nm) assembled through surface ions. Such self-assembly is widespread in multi-component complex fluids, paradoxically moderating hierarchical reactions. Stability and instability are not only critical but also complementary for co-optimisation around the nearby free energy landscape prior to bifurcation.

47 Globular pattern formation of hierarchical ceria nanoarchitecture

48

49

50

Introduction

51

52 Complex fluids with multiple components have attracted considerable attention over the last quarter of a
53 century, after the serendipitous discovery of their phase separation within biological cells and biomimic
54 systems.¹⁻³ For *in vivo* or *in vitro* molecular separations, concentration control is crucial.⁴⁻⁶ Meanwhile,
55 inorganic polymers exist in various phases, such as glasses, liquid crystals, and colloids.⁷⁻¹¹ Among these,
56 colloidal particles in liquid media like sol-gels have been of interest in engineering and fundamental
57 science, including soft condensed matter physics. However, comprehensive insight into multi-component
58 mixtures with strong or weak interactions remains challenging, particularly considering the balance of
59 colloidal particles dispersed and surrounded by labile ligands (*e.g.*, water, acid, or organic solvent)
60 undergoing rapid exchange reactions.

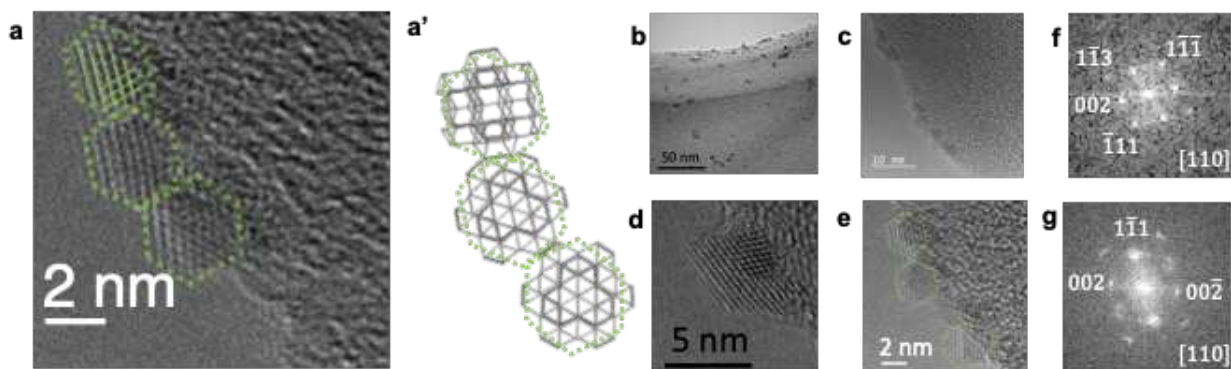
61 Water plays a special role in forming amorphous suspensions or precipitates of metal oxide ions due to
62 their rapid hydrolytic reactions. A closer examination of these materials reveals that metal aquo complexes
63 form direct bonds via hydroxo-bridging.^{12, 13} At equilibrium, deprotonation occurs within the complex.
64 The corresponding species are linked in successive equilibria to generate (hydr)oxide–metal clusters due
65 to the remarkable attraction among tetravalent heavy metal ions (Ce^{4+} , Th^{4+} , U^{4+} , Np^{4+} , and Pu^{4+}), even
66 at low pH.¹⁴⁻¹⁶ The generated hydroxide-bearing polymers often display disordered structures and
67 amorphous phases in the liquid state, and the crystallites grow from sub-micrometre sizes. With time, the
68 particle size increases by growth and agglomeration, and the particle size and structure in turn influence
69 the surface area of the nanostructured solid-state material. The solid phase is negatively charged due to
70 deprotonation, and thus, the surface moiety is surrounded by counter-cations. The resulting interparticle
71 repulsion mainly stems from the electrostatic force that competes with the attractive van der Waals force.¹⁷

72 Understanding the ion–surface interaction within these systems is critical, because these two opposing

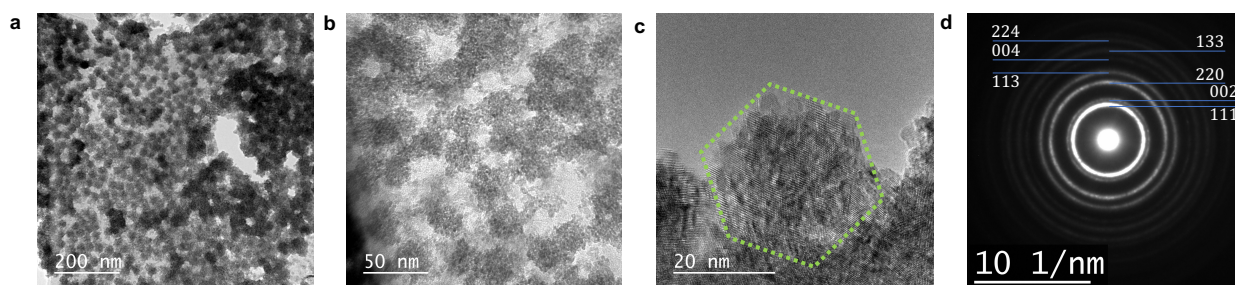
73 forces (attraction by hydroxides and repulsion by cations) are key to the design and control of nanoparticle
74 architecture in mesoscale engineering.

75 Here, we consider a representative system consisting of Ce^{4+} aquo ions, Ce^{IV} complexes, and Ce^{IV}
76 nanoparticles to reveal the intrinsically multiscale, hierarchical interaction when such nanostructures are
77 formed. Ceric ammonium nitrate (CAN) displays unique chemistry in organic solvents and water.^{18, 19} As
78 a strong oxidising agent, it is versatile in catalytic syntheses with acetonitrile, methanol, or acetone as the
79 typical media. The reaction requires less CAN than the equivalent amount of reactants and therefore does
80 not typically result in concentrated Ce^{4+} in the solution. Demars *et al.* reported that a Ce^{IV} oxo-bridged
81 dinuclear complex, viz. $[\text{Ce}^{\text{IV}}\text{-O-Ce}^{\text{IV}}]^{6+}$, is critical in catalysing C–O bond formation by accepting
82 electrons on two adjacent centres within the same complex.²⁰ Relatively simple geometries have been
83 reported for CAN in the organic phase, whereas its geometries in the aqueous phase are far more complex
84 due to multiple hydrolytic reactions, even at very acidic or under dilute conditions.^{21, 22} The vast majority
85 of experimental studies on CAN in water employ bottom-up approaches, starting from the monomer,
86 dimer, trimer, tetramer, hexamer, *etc.* Within these complexes, the hydroxyl group (OH^-) provides strong
87 linkages between two or three Ce^{4+} in various ways. Solid CeO_2 also contains this robust framework with
88 deprotonated OH^- groups. Ikeda-Ohno *et al.* distinguished double oxo-bridged dimers and large crystals
89 of CeO_2 using extended X-ray absorption fine structure (EXAFS) analysis.²² However, reports of
90 atomically precise CeO_2 nanocrystal synthesis remain limited.²³ Although researchers continue to fill gaps
91 in the cluster size from monomer, dimer, trimer, and hexamer to $\{\text{Ce}_{24}^{\text{IV}}\}$, $\{\text{Ce}_{38}^{\text{IV}}\}$, and $\{\text{Ce}_{40}^{\text{IV}}\}$,²¹⁻²⁶; that is,
92 the results remain incomplete. Another future research topic is controlling the aggregation of Ce^{IV}
93 nanoclusters. CAN possesses two equivalent moles of cation relative to one mole of anion, presenting a
94 typical multiscale system with charged ions or complexes, nanocrystal growth, and interactions among
95 colloidal particles (Fig. 1). This study aims to observe in real time the crystal seed formation and
96 aggregation toward CeO_2 nanoparticles in a CAN- HNO_3 solution and carry out the corresponding
97 modelling. The system involves two spatiotemporally different patterns that commonly emerge in

122 nanocrystalline structures with diffraction patterns consistent with the space group $Fm\bar{3}m$ (Figs. 2f and
 123 2g). Moreover, the lattice parameters $a = b = c = 0.541$ nm and $\alpha = \beta = \gamma = 90^\circ$ are common in numerous
 124 CeO_2 polycrystals.²⁸



125
 126 **Fig. 2** High-resolution transmission electron microscopy (TEM) images of CeO_2 -containing “primary” nanocrystals on
 127 the carbon-coated copper microgrid. The total concentration of added ceric ammonium nitrate is $C_{\text{Ce}^{IV}} \approx 0.50$ M in
 128 0.10 M HNO_3 . **a** TEM image at the highest resolution. **a'** Schematic drawing of the aggregate-flocculate (Sutherland’s
 129 ghost model). **b–c** TEM images at different resolutions. **d** A twin crystal. **e** TEM image displaying different aggregate-
 130 flocculate from that shown in **a**. **f–g** Selected area electron diffraction patterns indicating particle crystallinity. Scale
 131 bars: **a** 2 nm, **b** 50 nm, **c** 10 nm, **d** 5 nm, **e** 2 nm, **f** 10 nm^{-1} , and **g** 10 nm^{-1} .



132
 133
 134 **Fig. 3 a–c** Low-magnification TEM images of aggregated “secondary” clusters on the carbon-coated copper microgrid.
 135 The total concentration of added ceric ammonium nitrate was $C_{\text{Ce}^{IV}} = 50.0$ mM in 0.1 M HNO_3 . **d** Selected area
 136 electron diffraction pattern indicating particle polycrystallinity (the Debye-Scherrer ring). Scale bars: **a** 200 nm, **b** 50
 137 nm, **c** 20 nm, and **d** 10 nm^{-1} .

138
 139 These primary clusters do not appear to aggregate randomly, but rather exhibit a linear structure along the
 140 edge of the holey-carbon layer in the copper grid. Ball and Witten proposed the primitive Sutherland’s
 141 ghost model to distinguish two types of irreversible aggregation: the accretion of individual particles and
 142 the successive aggregation of clusters comparable in size.²⁹ The drying process used for sample

143 preparation was too rapid to deform these clusters, hence the irreversible aggregation. This step may lead
144 to the successive aggregation.^{30,31}

145 Conversely, at the lower concentration of $C_{Ce^{IV}} = 50.0$ mM in 0.1 M HNO₃, the TEM images reveal a
146 large architecture with 20–30 nm colloids (Figs. 3a–3c) forming an aggregate-flocculate of loosely bound
147 secondary particles. These colloids appear spherical or hexagonal (Fig. 3c) with sustained polycrystalline
148 structures (Fig. 3d for the single domain of a secondary particle in 3b). The genesis of the secondary
149 clusters is critical, because the TEM images only reveal these two nanoparticle types that are very different
150 in size. A closer examination of the colloidal sphere shows that the large particle is composed of
151 assembled primary particles (Fig. 2g), indicating strong cluster–cluster interactions in the liquid state,
152 whereas the sample’s nature changes during drying.

153 The same drying step was used at both $C_{Ce^{IV}}$ concentrations. The cluster–cluster aggregation is reversible
154 because the spatial distribution is random (Fig. 2b), instead of the successive formation of primary cluster
155 aggregates. Therefore, different interactions exist within the primary and secondary clusters. The
156 interaction between the charged primary clusters is due to the formation of a surface complex by hydroxo-
157 bridging or anion coordination. The surface potential (also known as the Nernst potential φ_0) of the
158 negatively charged secondary particle decays at a specific rate within the stagnant layer (the Stern layer,
159 with the potential of φ_s) in the presence of counter-cations such as H⁺ and NH₄⁺. The diffusive layer starts
160 at the outer boundary of the Stern layer. The shear plane (slipping plane) appears in the middle of the
161 diffusive layer. We attempted to measure the zeta potential ($\varphi = \zeta$), in addition to the effective
162 interparticle potential in the strong acid. However, the measurement failed because the 0.1 M HNO₃
163 corroded the copper electrode. Conversely, the secondary particles are sufficiently bulky and therefore
164 we could ignore their electrostatic interactions. The van der Waals potential, which decays at the rate of
165 r^{-6} , becomes dominant to initiate the inter-cluster aggregation to form the aggregate-flocculate pattern.

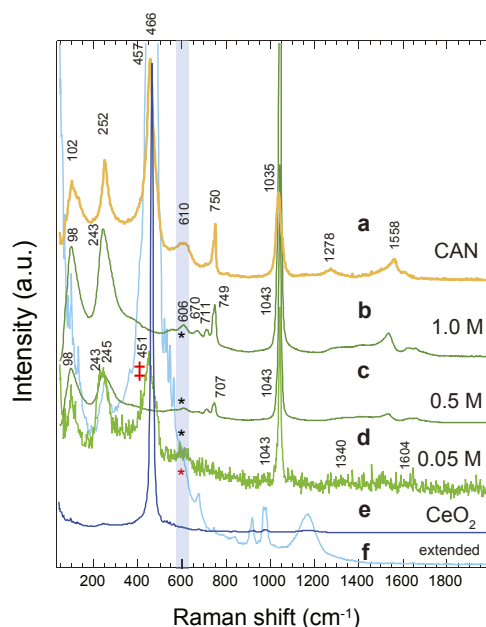
166 We then considered the driving forces to form the primary and secondary particles. The cluster-cluster
167 interaction, which led to colloidal growth from monodispersed nanocrystals to inter-cluster aggregates,

168 was considered.³² For the typical colloidal interaction, the classical Derjaguin-Landau-Verwey-Overbeek
169 (DLVO) theory^{17, 33} is based on the equilibrium of forces, such as the electrostatic force of the double
170 layer (dispersion repulsion) and the van der Waals forces (aggregation attraction). This theoretical model
171 contained at most two potential minima with a distance shorter than 1–5 nm. The first minimum decreased
172 in energy as the electrical double layer interaction between primary clusters became dominant, and the
173 second minimum appeared due to van der Waals attraction. At the surface of primary clusters, the
174 adsorbed ligands (NO_3^-) and counter ions (NH_4^+) were distributed within 5–10 nm, the local maximum
175 where the electrostatic repulsion is dominant. The van der Waals potential ($\propto r^{-6}$) was effective even at
176 more than ~ 10 nm, where the electrostatic potential ($\propto r^{-12}$) was negligible. Hence, the secondary-cluster
177 aggregation-flocculation occurred. While this CeO_2 system followed this rule, non-DLVO interactions
178 may be possible in hydroxo-bridging surface species, which is a type of structure effect specific to the
179 eigen shapes (non-spherical) of nanocrystals (such as primary clusters involving hundreds of Ce atoms).

180

181 **Raman spectroscopy.** Fig. 4 shows the Raman spectra of pristine CAN and CeO_2 , in addition to CAN
182 dissolved in 0.1 M HNO_3 at three different concentrations ($C_{\text{Ce}^{\text{IV}}} = 1.00, 0.50, \text{ and } 0.05$ M). All spectral
183 peaks for pristine solid-state CAN (spectrum **a** in Fig. 4) are assigned to well-known modes corresponding
184 to the vibrations of NO_3^- and $\text{Ce}^{\text{IV}}\text{-O-Ce}^{\text{IV}}$ (the “-O-” is from a bridging nitrate). The intense band at
185 252 cm^{-1} is assigned to the Ce-O-Ce vibration, and the weak bands at 750 and 1035 cm^{-1} are assigned
186 to nitrate bound to Ce^{4+} .²⁰ The most intense band in the spectrum of CAN at 457 cm^{-1} , which is located
187 close to the F_{2g} (T_{2g} symmetry) triply degenerate Raman-active mode of CeO_2 powder (466 cm^{-1}), does
188 not correspond to the solid-state pristine CAN or CAN- HNO_3 solutions (Figs. 4b, 4c, 4e, and 4f).³⁴⁻³⁶
189 Instead, this peak (457 cm^{-1}) corresponds to the F_{2g} mode. Considering the resolution under the
190 experimental condition ($\sim 4\text{ cm}^{-1}$), the two peaks at 457 and 466 cm^{-1} are certainly different with a non-
191 negligible phonon energy of 9 cm^{-1} . The bands at approximately 252 and 610 cm^{-1} in the spectra of CAN
192 powder and CAN solution at higher concentrations (spectrum **b** in Fig. 4) indicate non-negligible amounts

193 of oxygen vacancies compared to those within CeO_2 powder.³⁷⁻³⁹ These trends are especially remarkable
 194 in the batches containing the primary clusters. Conversely, at the relatively high concentrations of 1.00
 195 and 0.50 M, the Raman signals are more distinct than those in the spectra of the secondary clusters. The
 196 peak at 606 cm^{-1} on spectrum **d** in Fig. 4 indicates the crystalline structure of the primary clusters, and
 197 the scattering tensors of the band are A_{1g} , E_g , and F_{2g} .³⁵ This band was observed for all samples, although
 198 its intensity decreased at higher concentrations (labelled with “*” on spectra **b** and **c** in Fig. 4). Consistent
 199 with TEM (c.f. Fig. 2b), these batches contain the primary clusters as a significant component.
 200



201
 202 **Fig. 4** Raman spectra of CeO_2 -containing powder materials and CeO_2 -containing primary nanocrystals in HNO_3 . **a** Ceric
 203 ammonium nitrate (CAN) powder dried at $100\text{ }^\circ\text{C}$ for 3 h. CAN in 0.1 M HNO_3 at **b** $C_{\text{Ce}^{\text{IV}}} = 1.0\text{ M}$, **c** $C_{\text{Ce}^{\text{IV}}} = 0.5\text{ M}$, and **d**
 204 $C_{\text{Ce}^{\text{IV}}} = 0.05\text{ M}$. **e** As-received CeO_2 powder. **f** Spectrum of CeO_2 powder magnified in the y-direction to highlight the
 205 very weak peaks.
 206

207 Remarkably, the lower-energy band of nitrate displays multiple peaks (670 and 711 cm^{-1}) and is red-
 208 shifted for solutions at higher concentrations (spectra **b** and **c** in Fig. 4). The bound nitrate anion within
 209 pristine CAN favours bidentate coordination to one Ce^{IV} centre, with the vicinal hexa-nitrate sphere
 210 forming an icosahedral CeO_{12} core. The $[\text{Ce}(\text{NO}_3)_6]^{2+}$ has T_h (ideally O_h) molecular point group symmetry
 211 (shown in the monomer in Fig. 1). Notably, the Ce^{IV} complex commonly exhibits an isotropic structure.

212 After dissolution in acid, the coordination mode of the nitrate to Ce^{IV} changes from bi- to monodentate
213 due to primary cluster formation. Additionally, the nitrate is not bridging two Ce ions, and it is removed
214 from the core with the “[O–Ce–O]_{-n}” structure. Therefore, nitrate adsorption occurs on the core in a
215 mono- or bidentate fashion, generating two peaks at 710 and 670 cm⁻¹ that are red-shifted by ~40 and 80
216 cm⁻¹ from 750 cm⁻¹, respectively. The bands at 1035, 750, and 252 cm⁻¹ are assigned to NO₂ symmetric
217 stretching and bending and Ce–O stretching vibrations, respectively.^{20, 34, 40, 41}

218 The secondary clusters exhibit a unique spectral peak at 451 cm⁻¹ (indicated by the red “‡” in spectra **d**
219 in Fig. 4), which has not been reported thus far, although non-negligible peaks have been recorded at
220 approximately 606 cm⁻¹.²⁰ Based on a rough estimation of the particle size (58 nm), the band at 451 cm⁻¹
221 is associated with phonon coupling (Table 1). In samples with higher C_{Ce^{IV}} concentrations, this band
222 was not observed due to excess ammonium cations, resulting in the absence of secondary clusters (spectra
223 **b** and **c** in Fig. 4). Ce ion hydroxo-bridging causes the very weak, broad peaks at approximately 1340 and
224 1604 cm⁻¹. However, these peaks are non-negligible and remarkable for primary clusters, indicating
225 proton inclusion. The lowest-energy band at 98 cm⁻¹ may be due to Ce–Ce interactions. However, these
226 data are insufficient to identify either cluster type.

227 Meanwhile, we estimated the size of the single domain from the recorded Raman band width. We
228 employed this relationship to determine the appropriate domain size in the liquid state, including the
229 secondary cluster stability in a suspension. Weber *et al.* reported that particle-size effects influence the
230 spectral broadening in Raman scattering,³⁵ and the half-width of the Raman band has the following linear
231 relationship with the inverse crystalline size:

$$232 \quad \Gamma = a + (b/D), \quad (1)$$

233 where Γ (cm⁻¹) is the half-width at half-maximum of the observed Raman line, and D (nm) is the particle
234 radius. Given the empirical constants of $a = 5$ cm⁻¹ and $b = 51.8$ cm⁻¹/nm according to Weber *et al.*, we
235 obtained the particle sizes in Table 1 using this relationship. The obtained particle diameter (0.98 nm) is

236 comparable to those obtained using small-angle X-ray scattering (SAXS) (1.64 nm, to be discussed later).
 237 However, this approach is only applicable to primary clusters because they form a crystalline lattice.

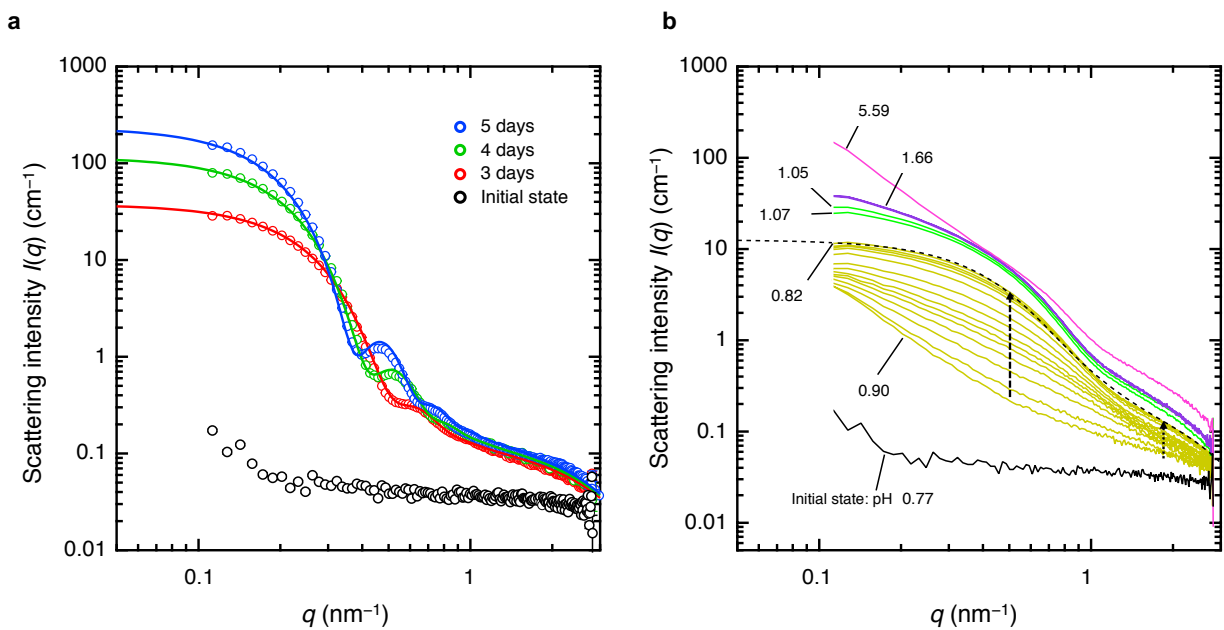
238

239 **SAXS.** SAXS is very informative, particularly for analysing the average physical properties of colloidal
 240 particles. Figs. 5a and 5b show the observed SAXS scattering intensity $I(q)$ for a solution containing $C_{Ce^{IV}}$
 241 = 50 mM in 1.0 M HNO_3 . Here, λ and 2θ are the wavelength of the incident X-ray and the scattering
 242 angle, respectively, and $q = (4\pi/\lambda) \sin \theta$ is the magnitude of the scattering vector. Fig. 5a displays the time
 243 evolution of SAXS patterns for the solution maintained at pH 0.771 for $t_0 = 0$ d (black circles), $t_1 = 3$ d
 244 (red circles), $t_2 = 4$ d (green circles), and $t_3 = 5$ d (blue circles) after sample preparation. The SAXS pattern
 245 at 0 d shows weak scattering intensity over a wide q range, indicating the absence of a nanoscale ordered
 246 structure in the solution. In sharp contrast, the patterns at ≥ 3 d indicate that an ordered structure appears
 247 spontaneously in the solution and grows with time. Specifically, the scattering intensity at low q
 248 ($q < 1.0 \text{ nm}^{-1}$) gradually increases with time, whereas that at high q ($q > 1.0 \text{ nm}^{-1}$) barely changes. There
 249 is no significant change at $t > 5$ d. These SAXS patterns come from two contributions: (i) $I_p(q)$ at $q > 1.0$
 250 nm^{-1} due to the primary clusters of the m -mer $\{Ce_m^{IV}\}$, and (ii) I_s at $q < 1.0 \text{ nm}^{-1}$ due to the aggregates
 251 (secondary clusters). Therefore, the mean size of the secondary clusters likely increases with time,
 252 whereas that of small clusters remains almost constant. The SAXS patterns are reproduced by summing
 253 I_p and I_s , which assume the form factor of spherical particles with the respective radii of R_p and R_s :

$$254 \quad I(q) = A \left[\frac{3 \{ \sin(qR_p) - (qR_p) \cos(qR_p) \}}{(qR_p)^3} \right]^2 + B \left[\frac{3 \{ \sin(qR_s) - (qR_s) \cos(qR_s) \}}{(qR_p)^3} \right]^2, \quad (2)$$

255 where A and B are proportionality constants. The R_s distribution is considered to precisely reproduce the
 256 SAXS intensity distribution. Thus, we use a Gaussian distribution with standard deviation σ_R , while the
 257 R_p distribution is ignored because of the invisibility of the region of $q > \frac{1}{R_p}$ in Fig. 5a. The solid lines in
 258 Fig. 5a represent the best-fit theoretical scattering curves using Eq. (2) with the refined parameters listed
 259 in Table 2. R_p is constant at approximately 0.8 nm regardless of t , whereas R_s increases from 9.2 nm at t_0

260 = 0 min to 12.3 nm at $t_1 = 3$ d. Remarkably, the first peak of $I_s(q)$ observed at $q \approx 0.5$ nm becomes sharper
 261 with t . Moreover, $\frac{\sigma_R}{R_s}$ changes from 0.14 (3 d) to 0.10 (5 d), indicating transformation of the particle shape
 262 to a more spherical (or highly symmetrical) structure due to spatial rearrangement of the primary clusters
 263 within the aggregates. Hence, colloidal aggregation proceeds while maintaining the primary cluster size.
 264 Additionally, the crystal growth of primary particles and cluster-cluster aggregation are at non-
 265 equilibrium during the observation period of several hours.²¹
 266



267

268 **Fig. 5** Double-logarithmic plots of the small-angle X-ray scattering (SAXS) patterns ($I_{\text{obs}}(q)$ vs. q). **a** Profiles as a
 269 function of time for $C_{\text{Ce}^{\text{IV}}} = 50.0$ mM in 1.0 M HNO₃. The solid line is the best-fit theoretical line obtained using Eq. (2)
 270 combined with the characteristic parameters listed in Table 2. **b** SAXS profiles at different pH levels adjusted using
 271 NaOH (50 wt.% ≈ 19.7 M). The line colours (pH values) are: magenta (5.59), purple (1.66), green (1.05, 1.070), yellow
 272 (0.90–0.82), and black (0.77). The yellow lines were measured at 20-min intervals.

273

274

275 **Titration trends.** We observed the colloidal behaviour of the system near equilibrium⁴², including
 276 nanocrystal aggregation and the growth of these nanocrystals upon addition of a strong alkaline solution
 277 to alter the pH. Fig. 5b shows SAXS patterns obtained during the titration of CAN ($C_{\text{Ce}^{\text{IV}}} = 50$ mM) in
 278 1.0 M HNO₃ using 19.7 M NaOH. During titration, the pH increases from 0.77 to 5.59. Prior to NaOH

279 addition (pH 0.77), the weak scattering intensity (black line) indicates no ordered structure, and this SAXS
280 pattern is identical to the initial state in Fig. 5a. Upon adding the first droplet of concentrated NaOH (2
281 μL) to 1.0 mL of CAN solution, the pH increases to 0.901, with an immediate, severe change in the SAXS
282 pattern (yellow lines). The SAXS intensity increases with decreasing q , resulting in the power-law
283 scattering of $I(q) \sim q^{-2}$ at $q < 0.5 \text{ nm}^{-1}$, which indicates the formation of large aggregates that may be
284 linked to promoted hydrolysis at higher local pH. After another 3.5 h, the pH gradually decreases to 0.82,
285 and the SAXS intensities at approximately $q = 0.5$ and 2.0 nm^{-1} gradually increase to form two shoulders
286 (indicated by dashed arrows). This suggests a hierarchical ordering within the solute, specifically the
287 primary clusters and secondary aggregates.

288 The SAXS pattern at pH 0.82 (top yellow line) is reproduced using Eq. (2) with the refined parameters
289 $R_p = 0.85 \text{ nm}$, $R_s = 5.31 \text{ nm}$, and $\sigma_R = 1.51 \text{ nm}$, as indicated by the best-fit theoretical profile (black dashed
290 line). R_s becomes less than half of that in Fig. 5a, whereas R_p shows good agreement. Remarkably, in the
291 SAXS patterns the first peak of $I_s(q)$ was not observed due to a broad distribution ($\frac{\sigma_R}{R_s} = 0.28$), suggesting
292 that the primary cluster configuration within the secondary aggregates likely persists, even in a metastable
293 state.

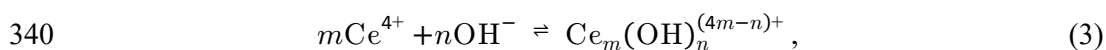
294 The second droplet of NaOH (6 μL) induces an abrupt increase in pH from 0.90 to 1.07. Accordingly, the
295 SAXS intensity increases without significant changes in the q dependence (lower green line). The SAXS
296 pattern does not change without further addition of NaOH, though the solution pH decreases to 1.06 after
297 12 h (top green line). The third droplet of NaOH (4.5 μL) adjusts the pH to 1.66 and induces a slight
298 increase in the scattering intensity at $q < 0.4 \text{ nm}^{-1}$ while maintaining that at $q > 0.4 \text{ nm}^{-1}$ (purple line).
299 This indicates further aggregation among the secondary aggregates. The pH changes very little with time
300 (barely on the order of 0.01) for each short SAXS measurement. After adding a fourth NaOH droplet
301 (1.5 μL , pH 5.59), the scattering intensity at $q < 0.4 \text{ nm}^{-1}$ increases dramatically (pink line) while the
302 shoulder peak at $q \approx 2.0 \text{ nm}^{-1}$ remains, suggesting primary clusters within the system. At this high pH,
303 the solution becomes turbid due to $[\text{Ce}(\text{OH})_4]_n$ formation, finally forming a muddy precipitate.

Discussion

304

305 Our main aim was to understand the two hierarchically different intra/interparticle interactions governing
306 the particle shapes. The primary cluster grows as a single crystalline phase following initial seed
307 nucleation in the acidic solution. The first concern is whether the CeO₂ nanocrystal grows through the
308 connection of building blocks based on Ce–(OH)–Ce bonding, including subsequent deprotonation to
309 form the solid oxides. This hypothesis may lead to “proton ambiguity”—the difficulty of establishing the
310 origin of a released proton experimentally.⁴³ Hence, an approach combining spectroscopic techniques
311 (EXAFS analysis and Raman spectroscopy) with theoretical calculations such as density functional theory
312 (DFT) and molecular dynamic simulation is appropriate. Ikeda-Ohno *et al.* confirmed dinuclear complex
313 formation using EXAFS analyses and DFT calculations.²² The protons on the double hydroxo-bridge
314 between two Ce ions are predominantly present within [Ce^{IV}₂(μ₂-OH)₂(H₂O)₁₄]⁶⁺.²² The monomer-to-
315 dimer complex formation is the nucleation step, followed by reaction limited aggregation (RLA) that
316 could continuously build up the molecular blocks and form nano primary clusters (Fig. S1c). Concerning
317 clusters, Mitchel *et al.* compared a distorted CeO₂ nanocrystal structure to the bulk and found slight
318 disorder in the boundary lattice structure.²³ Their finding suggests that excess protons or defects may exist
319 within the crystal structure of pure CeO₂. The characteristic Raman band at 451 cm⁻¹ is common for
320 condensed ensembles and the sample with C_{Ce^{IV}} = 0.05 M, but the assignment of this band remains unclear
321 (Fig. 4d) because it was not observed for the samples with C_{Ce^{IV}} = 1.0 and 0.5 M. Conversely, the band
322 also appears very specific to a chemical bond formed within the coarse-grained clusters. One plausible
323 assignment is a phonon band associated with the monodispersed colloidal particles. Herein, the Raman
324 spectrum reveals a mean particle size of 0.98 nm, which is roughly comparable to 1.68 nm (Table 1).
325 Based on these findings, the average number of Ce atoms in the primary cluster is $\bar{n} \sim 10^2$. Reported
326 chemical species in the literature range from the monomer complex to a 40-mer as one of the metastable
327 groups,^{20, 21, 23} in which the crystal growth almost stops at a certain level of reaction due to structural
328 optimization across the local free energy landscape. This is essential for understanding primary clusters
329 that appear by chemical reaction. (The fraction for each particle size is given in Fig. S1c). Therefore, 24-,

330 38-, and 40-mers are not magic numbers by the assumption of a continuous distribution of \bar{m} ; additionally,
 331 single crystals with a slightly larger \bar{m} could be isolated because they are more stable and form a vast
 332 majority in complex fluids. In terms of RLA, it is significant to extend the chemical reaction model to
 333 include the self-assembly of primary clusters. The nucleation and crystal growth of CeO₂ nanoparticles in
 334 HNO₃ solution was observed at different solution pH. When the orange-coloured CAN powder dissociates
 335 in an acidic solution, Ce⁴⁺ forms various complexes with NO³⁻, H₂O, and OH⁻ generated by water
 336 dissociation. During seed crystal nucleation, the bridging ligand is significant because direct Ce^{IV}-Ce^{IV}
 337 interaction is unfavourable in aqueous solutions. The hydrolysis may lead to the corresponding nucleation,
 338 and the nitrate anion is unlikely to bridge donors except in the solid state. A higher pH drives the following
 339 reaction equilibrium to the right:

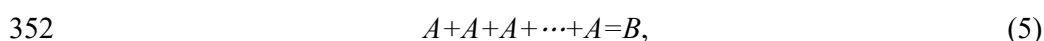


341 where $m = 1$ and $n = 0-4$. Details about our modelling is described in the Methods section as *self-assembly*.
 342 Now, we discuss the secondary clusters. We compare two models to describe the aggregation and
 343 dispersion properties of the clusters in order to clarify which one is more appropriate for our system. The
 344 aggregation-fragmentation dynamics for active clusters was described by Ginot *et al.*⁴⁴ In their model, the
 345 cluster size distribution (denoted by C_N) starts from a binary reaction in the simplest formula:

$$346 \quad \frac{C_N}{C_3} = \left[\prod_{m=4}^N \frac{C_1 A_{m-1}}{F_m} \right] = \frac{\kappa^{N-3}}{\sqrt{N(N-1)(N-2)/6}}, \quad (4)$$

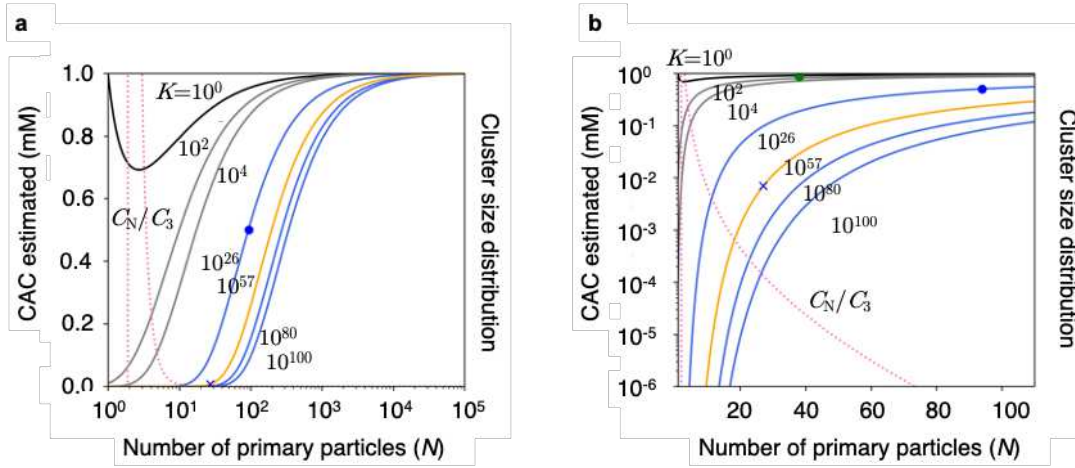
347 where C_1 is a normalisation constant and N is the number of primary particles. Finally, the cluster size
 348 distributions shown in Figs. 6a and 6b (pink dotted curves) satisfy Eq. (4) with $\kappa = 0.50/0.52$.⁴⁴ The model
 349 covers C_3 as a minimum.

350 Conversely, one assumes secondary cluster (B) aggregation using the simplest scheme for self-assembled
 351 micelles:



353 where A is the monomer of the primary cluster. The reaction equilibrium constant is $K = X_B/X_A^N$.
 354 Assuming $C = X_A + NX_B$ where X_A and X_B are the respective molar fractions, we obtain

355
$$X_A = \sqrt[N]{\frac{C - X_A}{NK}} . \quad (6)$$



356
 357 **Fig. 6** Numerical curves of the critical aggregation concentration (CAC) for hierarchical nanoarchitectures as a
 358 function of the number of primary particles (N). Pink dotted curves are the cluster size distributions of secondary
 359 particles (converted using the analysis of Ginot *et al.*⁴⁴). The curves are calculated using $CAC = f_N = (NK)^{-1/N}$. **a** shows
 360 the overall trend and **b** shows the expanded view. Blue “x”: primary clusters, green square: secondary clusters. K is the
 361 equilibrium constant for secondary cluster formation.

362
 363 When $K \gg 1$ and $C \gg 1$, we have

364
$$X_A \leq \sqrt[N]{\frac{1}{NK}} =: f_N . \quad (7)$$

365 In Figs. 6a and 6b, we compare the f_N curves at $K = 10^0, 10^2, 10^4, 10^{80},$ and 10^{100} . The critical aggregation
 366 concentration (CAC) reflects the transition between the primary and secondary clusters. Because this
 367 conventional model assumes $K \gg 1$, the values of 10^0 and 10^2 are not appropriate. This model does not
 368 consider secondary cluster fragmentation, thus simply yielding the speculated maxima curves for CAC.
 369 The primary and secondary clusters exhibit intrinsically different CACs.

370 Meanwhile, we calculate the secondary cluster concentration as $C_s = 6.97$ mM (for details, see SI). The
 371 remaining Ce^{IV} ($C_i = 43.0$ mM) includes ionic species and primary clusters in the medium. Furthermore,

372 the mean aggregation number of the secondary clusters is $\bar{n} = 27.0$ from Fig. 6a (green circle). This is
373 likely close to very low K , suggesting that the secondary clusters are loosely coupled together because the
374 reaction is near equilibrium. The blue filled circle in Fig. 6b, where the two models (i.e., curves with pink
375 dots and 10^{100}) cross, yields $\bar{n} \sim 27$ (see SI in detailed calculation) and CAC ~ 0.20 mM. This CAC
376 seems an underestimation. An exact solution must exist upwards from there: $K \sim 10^{57}$ and $K \sim 10^{26}$ are
377 plausible equilibrium constants for the secondary and primary clusters, respectively, assuming that the
378 observed $\bar{n} = 27.0$ is the critical aggregation condition. Yet, this system is not completely elucidated
379 without a precisely determined K , which is obtained by conversion from Gibbs free energy. The
380 challenges in phase transformation should be addressed in future work.

381 More importantly, static consideration from the classical DLVO theory indicates that the secondary
382 cluster is stabilised near the global minimum. However, many factors—e.g. rheological terms such as
383 spatiotemporal heterogeneity of the strongly alkaline droplet, vigorous stirring, heat distribution,
384 boundary condition—affect efficient energy transport in a multi-component complex fluid. Therefore, the
385 approach considering diffusion limited aggregation (DLA) may be a more realistic pathway to transit via
386 saddles or nodes on the free energy landscape of such a dynamic system. In fact, our *in-situ* real-time
387 observation supports the idea of a chaotic system: the system falls into a limit cycle behaviour⁴⁵ under
388 many conditions, and the only difference is when to participate. These factors induce the system of
389 secondary clusters into a non-equilibrium state specified as *near equilibrium*.⁴⁶

390 Besides the kinetic process, the fluctuation of water and water-related species is critical for fully
391 describing the entire system involving local diffusion of primary and secondary particles by Brownian
392 motion,⁴⁷ potentially through a free hydroxide ion.⁴⁸ Furthermore, the dissipative structure is key to
393 understanding mixed liquid-solid systems. However, these are just speculations at this time, and the
394 validity of these theories should be checked in our subsequent work. The explanation for the hierarchical
395 structure formation may be the surface free energy change under different conditions. This appears
396 slightly paradoxical; and the present result represents a typical example within the Lyapunov stability⁴⁶

397 Self-assembly is ubiquitous in multi-component complex fluids, which paradoxically moderates the
398 hierarchical reactions. Stability and instability are not only critical but complementary for co-optimisation
399 in the nearby free energy landscape prior to bifurcation. Remarkably, Smarsly *et al.* recently reported
400 CeO₂ colloidal particles similar to ours and proposed the synthetic pathways for particle formation.⁴⁹
401 However, their advanced work only characterised the agglomerates as products *via* their original protocols
402 and did not perform *in-situ* observation of the secondary clusters. In this respect, the present study is not
403 a simple extension of prior work, since it mainly focuses on the hierarchical structure itself via *in-situ*
404 observation using high-resolution TEM and Raman spectroscopy. This approach enables us to cover the
405 concentrations ranging from 10⁻³ to 10⁰ M, which are common conditions in condensed soft matter such
406 as a living cell. However, it remains unclear how to explain the hierarchical governance in the multi-
407 component mixture to reach an energetically relaxed state. subsequent studies on the boundary between
408 equilibrium and nonequilibrium may have significant potential impact in nanoscience. Note that our
409 model does not directly deal with a hierarchical structure. Rather, it only describes the relationship
410 between two different scales. Scaling theory and renormalisation group approaches developed in the field
411 of condensed matter physics may render further insight. Additionally, it is theoretically possible to
412 investigate the concomitant interaction within the hierarchical nanoarchitecture by calculating the force
413 curves using state-of-the-art molecular simulations, which was not pursued in this study.

414 In summary, we conducted *in-situ* real-time observation of hierarchical CeO₂ nanoarchitectures formed
415 from CAN in acidic solutions. Such observations of colloidal particles on a wide scale have rarely been
416 reported. SAXS and TEM were used in combination to verify the formation of a hierarchically assembled
417 structure as a quasi-ceria colloid. The primary core clusters were 1–3 nm in size and composed of
418 nanocrystals, while the secondary clusters were colloids 20–30 nm in size. Moreover, the secondary
419 clusters exhibited colloidal aggregation and dispersion, which could be statically explained by the
420 classical DLVO theory. The novelty in the present work is a reconsideration of the classical model in
421 order to understand the dynamics by DLA approach, which explains the present results well. In such a
422 multi-phase mixture, the complementary reactions of primary cluster formation at equilibrium and

423 secondary cluster formation at near equilibrium represent a *live-and-let-live* principle to maintain a global
424 efficient free energy network in the system. The dissipative structure and corresponding fluctuation may
425 be critical in controlling this slow reaction. These results may provide a simple explanation for the
426 geometrical structures of oligomeric complexes in solutions, although larger assembled structures in a
427 complex fluid are more crucial for the development of Ce-based materials. This study using CeO₂
428 nanoparticles in a complex fluid is relevant to many other systems, and the results has substantial
429 implications for colloid chemistry and non-equilibrium physics.

430

431

432

433

434

435

436

437

438

439

440

441

442

443

444

445

446

447

448

Methods

449

450 **Samples.** Commercially available CAN (purity >98%, Tokyo Chemical Industry Co., Ltd., Tokyo, Japan)
451 was placed in an oven at 110 °C overnight to remove the physisorbed water. Concentrated HNO₃ (69 wt.%,
452 Wako Pure Chemical Industries, Ltd., Osaka, Japan) and NaOH (50 wt.% solution, Wako Pure Chemical
453 Industries, Ltd.) were diluted in milli-Q water for use as titrants during SAXS. For TEM, a droplet of
454 CAN solution was placed on a copper microgrid (carbon-reinforced STEM 150Cu grid, Okenshoji Co.,
455 Ltd., Tokyo, Japan) and dried overnight at approximately 20 °C. For Raman microscopy analysis, pristine
456 microcrystalline powders of dehydrated CAN and CeO₂ (Wako Pure Chemical Industries, Ltd., >99.9%)
457 were mounted on a carbon seal. The CeO₂ particle size in 0.1 M HNO₃ was determined using a zetasizer
458 (Zetasizer Nano, Malvern Panalytical, Malvern, UK) to be 83.4 nm for monomers and 354.7 nm for
459 aggregates. Raman spectra were also collected for liquid samples placed on a glass plate.

460

461 **Procedure and apparatus.** The formed hierarchical structures were examined in two CAN solutions with
462 the total concentrations of $C_{\text{Ce}^{\text{IV}}} = 500$ and 50 mM, denoted as the first and second series, respectively.
463 TEM (JEM-2100F, JEOL Ltd., Akishima, Tokyo, Japan; operating at 200 kV),⁵⁰ Raman microscopy
464 (Micro-Ram 300, Lambda Vision Inc.), and SAXS (Rigaku, Tokyo, Japan) analyses were used to obtain
465 important information about the samples. The micro-Raman spectrometer was equipped with a 532-nm
466 Nd:YAG laser focused onto the sample using a 100 × objective lens, and laser power at the sample
467 position was 32 mW. The Raman spectra were recorded in the range 50–1970 cm⁻¹ with a spectral
468 resolution of 4 cm⁻¹ and an acquisition time of 10 s. Each spectrum consisted of five accumulations
469 acquired for each sample. Background subtraction was not performed. Raman spectroscopy was suitable
470 at high concentrations of $C_{\text{Ce}^{\text{IV}}} = 0.50$ and 1.00 M, where SAXS was no longer appropriate.

471

472 **SAXS.** SAXS was performed using an X-ray diffraction apparatus (NANO-Viewer, Rigaku). The incident
473 Cu K α radiation ($\lambda = 0.154$ nm) was focused on a spot 450 μm in diameter on the sample with a confocal

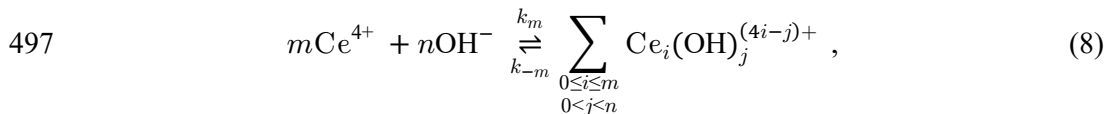
474 optic (Max-Flux, Rigaku) equipped with a pinhole slit collimator. A two-dimensional (2D) position-
 475 sensitive detector (PILATUS 100K/R, Rigaku) of 195×487 pixels with a spatial resolution of 0.172
 476 mm/pixel was used to record X-rays scattered from the sample. The magnitude of the scattering vector
 477 (q) was between $0.1\text{--}2.8 \text{ nm}^{-1}$ at two sample-to-detector distances of 92 and 655 mm, as determined by q
 478 $= (4\pi/\lambda)\sin\theta$ ($2\theta =$ scattering angle). We corrected the scattering data for the counting efficiency,
 479 instrument background, and air scattering on a pixel-to-pixel basis.⁵¹ The X-ray scattering intensity
 480 distribution was circularly averaged and converted to an absolute unit of the scattering intensity (cm^{-1})
 481 by calibration with water scattering.⁵² The corrected scattering intensity was designated as $I(q)$, and then
 482 the cell scattering was subtracted from $I(q)$ by considering the transmission. The sample solution was
 483 loaded using a peristaltic pump into a titanium cell with a thickness of 1.25 mm (path length) and quartz
 484 plate windows ($6.0 \text{ mm} \times 2.5 \text{ mm} \times 0.02 \text{ mm}$).^{51, 53} All X-ray scattering data were acquired at $25 \text{ }^\circ\text{C}$.

485

486 **Computer software.** Molecular modelling was carried out using UCSF Chimera package
 487 (www.cgl.ucsf.edu/chimera/).⁵⁴ The CAC curves were produced using matplotlib and seaborn v0.8.1.⁵⁵
 488 Some of the images and videos were generated using CrystalMaker[®] 10.5.4 (www.crystallmaker.com).
 489 The SAXS patterns were analysed using Igor Pro (Wavemetrics, Lake Oswego, OR, USA).

490

491 **Theory and reaction modelling.** For the hydroxo-bridging ligands such as $\mu\text{-OH}$ and $\eta\text{-OH}$, SAXS
 492 revealed a hierarchical structure with an aggregated shape of rigid globules, because the primary and
 493 secondary clusters grew at different rates. To the best of our knowledge, such results have not been reported
 494 in the literature except for Smarsly *et al.*,⁴⁹ possibly due to a lack of advanced techniques or interest. Ions,
 495 complexes, dimers, trimers, 38- and 40-mers, *etc.*²³ and their aggregates co-exist in a single solution.
 496 Therefore, we extend Eq. (3) as follows:



498 with

$$499 \quad \sum_{\substack{0 \leq i \leq m \\ 0 < j < n}} \text{Ce}_i(\text{OH})_j^{(4i-j)+} := \{\text{Ce}_1\} + \{\text{Ce}_2\} + \{\text{Ce}_3\} + \dots + \{\text{Ce}_i\} + \dots + \{\text{Ce}_{38}\} + \dots + \{\text{Ce}_m\}, \quad (9)$$

500 where the kinetic constants $k_m \geq k_{-m}$, and $\{\text{Ce}_i\}$ denotes the i -mer of hydroxo-species. Solid-state CeO_2
 501 is formed in the limit of $m \rightarrow \infty$, yielding the irreversible kinetic constants $k_m \gg k_{-m}$.

502 The assumption $a_i = \{\text{Ce}_i\}$ holds when all species exist in equimolar fractions. Considering the cluster-
 503 cluster dimer, we approximate Eq. (9) by the *self-assembly reaction*:

$$515 \quad \sum_{\substack{0 \leq i \leq m \\ 0 < j < n}} \text{Ce}_i(\text{OH})_j^{(4i-j)+} \sim \left(\sum_i a_i \right) - \mathcal{O} \left(g \left(\binom{m}{k} \right) \right), \quad (10)$$

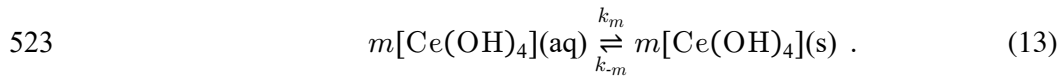
504 where $\mathcal{O} \left(g(X^k) \right)$ is the Bachman-Landau \mathcal{O} -notation of the function $g(x)$, and $X^k = \binom{m}{k}^k$ is the k^{th} order
 505 of a binomial distribution. The conventional solution chemistry approximates the equilibria in a dilute
 506 solution. The first term in the summation on the right side of Eq. (10) considers the formation of
 507 multinuclear species with equivalent or different numbers of OH^- . The second term with the \mathcal{O} -notation
 508 represents the order of reaction, including the probability of collision between two primary clusters. The
 509 second term in eq(10) becomes non-negligible when interparticle interaction is dominant, resulting in the
 510 aggregation of k particles out of a total of m particles. Here, the solution is close to a regular one, and
 511 thus the second term on the right is no longer negligible and potentially becomes dominant. Thus, we
 512 adopt a modelling approach suitable for aggregation–fragmentation dynamics, and compare this model
 513 with the classical model that approximates the system’s conditions. Taken together, these models should
 514 cover the two-rank hierarchical system.

516 Meanwhile, the SAXS data during titration contain a counterintuitive feature: when more base is added,
 517 the pH decreases instead of increases. Assuming $n = 4m$ in Eq. (10), we consider the formation of the
 518 solid phase:





521 In our system, the kinetic constant k_1 in Eq. (12) is too large to be experimentally measurable. Instead,
522 the following metal ion polymerisation presumably emerges as primary cluster nucleation:



524 Equation (13) explains non-equilibrium in the classical thermodynamic description for a sufficiently large
525 m . However, it could not possibly occur on the atomic scale. The SAXS patterns in the high- q range
526 ($q > 1.0$) remain almost intact or show a little reduction in terms of $I(q)$ as a function of t (data represented
527 by open circles in Fig. 5a). This supports the literature descriptions regarding nanocrystalline CeO_2
528 solubility.⁵⁶

529

530

531 **Data Availability:** The authors confirm that the data supporting the findings of this study are available
532 within the article and its supplementary material.

533

534

535

536

537

538

539

540

541

542

543

544

Tables

545 Table 1 Summary of particle diameters measured using different methods, and the half-width at half maximum
 546 (HWHM) used to calculate the particle diameter using Raman band widths and Eq. 1.

547

| Sample | Particle diameter (nm) | | | | HWHM (cm ⁻¹) at 466 nm |
|------------------|------------------------|------------------|---------|--------|---------------------------------------|
| | SAXS | TEM | Raman | Others | |
| CAN | — | — | | 2.59* | 25.0 |
| 1.00 M | Not measured | p: 1–3 | N. A. | | Not observed |
| 0.50 M | p: 1.64 | p: 1–3 | N. A. | | Not observed |
| 0.05 M | p: 1.68, s: 24.6 | p: 1–3, s: 20–30 | p: 0.98 | | 58.0 |
| CeO ₂ | — | — | | 35.5** | 5.71 |

548 *calculated from the empirical line, **measured by dynamic light scattering. p: primary cluster, s: secondary cluster.

549 CAN, ceric ammonium nitrate; SAXS, small-angle X-ray scattering; TEM, transmission electron microscopy.

550

551 Table 2 Summary of the parameters of hierarchical aggregates determined by analysis of the small-angle X-ray
 552 scattering intensity $I(q)$.

| t (days) | R_p (nm) | σ_p (nm) | R_s (nm) | σ_s (nm) |
|----------|------------|-----------------|------------|-----------------|
| 3 | 0.82 | 0.22 | 9.24 | 1.29 |
| 4 | 0.83 | 0.22 | 11.17 | 1.31 |
| 5 | 0.84 | 0.21 | 12.41 | 1.29 |

553 R_p , radius of primary spherical particle; R_s , radius of secondary spherical particle; σ_p and σ_s are the respective standard
 554 deviations.

555

556

557

558

559

560

561

562

563

564

- 567 1. Brangwynne CP, *et al.* Germline P Granules Are Liquid Droplets That Localize by Controlled
568 Dissolution/Condensation. *Science* **324**, 1729 (2009).
569
- 570 2. Li P, *et al.* Phase transitions in the assembly of multivalent signalling proteins. *Nature* **483**, 336-
571 340 (2012).
572
- 573 3. Shin Y, Brangwynne CP. Liquid phase condensation in cell physiology and disease. *Science* **357**,
574 eaaf4382 (2017).
575
- 576 4. Dixit S, Crain J, Poon WCK, Finney JL, Soper AK. Molecular segregation observed in a
577 concentrated alcohol–water solution. *Nature* **416**, 829-832 (2002).
578
- 579 5. Onuki A. *Phase Transition Dynamics*. Cambridge University Press (2002).
580
- 581 6. Doi M. *Soft matter physics* (2015).
582
- 583 7. De Yoreo JJ, *et al.* Crystallization by particle attachment in synthetic, biogenic, and geologic
584 environments. *Science* **349**, aaa6760 (2015).
585
- 586 8. Motokawa R, *et al.* A Telescoping View of Solute Architectures in a Complex Fluid System.
587 *ACS Cent Sci* **5**, 85-96 (2019).
588
- 589 9. Aoyagi N, *et al.* Photophysical Property of catena-Bis(thiocyanato)aurate(I) Complexes in Ionic
590 Liquids. *Cryst Growth Des* **15**, 1422-1429 (2015).
591
- 592 10. Colliard I, Morrison G, Loye H-Cz, Nyman M. Supramolecular Assembly of U(IV) Clusters and
593 Superatoms with Unconventional Counteranions. *J Am Chem Soc* **142**, 9039-9047 (2020).
594
- 595 11. Aoyagi N, *et al.* Thermochromic properties of low-melting ionic uranyl isothiocyanate
596 complexes. *Chem Commun* **47**, 4490-4492 (2011).
597
- 598 12. C. F. Baes and R. S. Mesmer: The Hydrolysis of Cations. John Wiley & Sons, New York,
599 London, Sydney, Toronto 1976. 489 Seiten, Preis: £ 18.60. *Berichte der Bunsengesellschaft für*
600 *physikalische Chemie* **81**, 245-246 (1977).
601
- 602 13. Aoyagi N, Palladino G, Nagasaki S, Kimura T. Optical Properties of Trinuclear Citrate
603 Complexes Containing 4f and 5f Block Metals. *Bull Chem Soc Jpn* **91**, 882-890 (2018).
604
- 605 14. Martin NP, *et al.* {Np38} clusters: the missing link in the largest poly-oxo cluster series of
606 tetravalent actinides. *Chem Commun* **54**, 10060-10063 (2018).
607
- 608 15. Martin NP, *et al.* Formation of a new type of uranium(iv) poly-oxo cluster {U38} based on a
609 controlled release of water via esterification reaction. *Chem Sci* **9**, 5021-5032 (2018).
610
- 611 16. Toraishi T, Farkas I, Szabó Z, Grenthe I. Complexation of Th(iv) and various lanthanides(iii) by
612 glycolic acid; potentiometric, 13C-NMR and EXAFS studies. *J Chem Soc Dalton Trans*, 3805-
613 3812 (2002).

- 614
615 17. Israelachvili JN. 6 - Van der Waals Forces. In: *Intermolecular and Surface Forces (Third*
616 *Edition)* (ed Israelachvili JN). Academic Press (2011).
617
- 618 18. Nair V, Balagopal L, Rajan R, Mathew J. Recent Advances in Synthetic Transformations
619 Mediated by Cerium(IV) Ammonium Nitrate. *Acc Chem Res* **37**, 21-30 (2004).
620
- 621 19. Nair V, Deepthi A. Cerium(IV) Ammonium Nitrate A Versatile Single-Electron Oxidant. *Chem*
622 *Rev* **107**, 1862-1891 (2007).
623
- 624 20. Demars TJ, Bera MK, Seifert S, Antonio MR, Ellis RJ. Revisiting the Solution Structure of Ceric
625 Ammonium Nitrate. *Angew Chem Int Ed* **54**, 7534-7538 (2015).
626
- 627 21. Ikeda-Ohno A, Hennig C, Weiss S, Yaita T, Bernhard G. Hydrolysis of tetravalent cerium for a
628 simple route to nanocrystalline cerium dioxide: an in situ spectroscopic study of nanocrystal
629 evolution. *Chem Eur J* **19**, 7348-7360 (2013).
630
- 631 22. Ikeda-Ohno A, Tsushima S, Hennig C, Yaita T, Bernhard G. Dinuclear complexes of tetravalent
632 cerium in an aqueous perchloric acid solution. *Dalton Trans* **41**, 7190-7192 (2012).
633
- 634 23. Mitchell KJ, Abboud KA, Christou G. Atomically-precise colloidal nanoparticles of cerium
635 dioxide. *Nat Commun* **8**, 1445 (2017).
636
- 637 24. Hennig C, *et al.* Crystal Structure and Solution Species of Ce(III) and Ce(IV) Formates: From
638 Mononuclear to Hexanuclear Complexes. *Inorg Chem* **52**, 11734-11743 (2013).
639
- 640 25. Marsac R, Réal F, Banik NL, Pédrot M, Pourret O, Vallet V. Aqueous chemistry of Ce(iv):
641 estimations using actinide analogues. *Dalton Transactions* **46**, 13553-13561 (2017).
642
- 643 26. Antonio MR, Ellis RJ, Estes SL, Bera MK. Structural insights into the multinuclear speciation of
644 tetravalent cerium in the tri-n-butyl phosphate–n-dodecane solvent extraction system. *Physical*
645 *Chemistry Chemical Physics* **19**, 21304-21316 (2017).
646
- 647 27. Jullien R, Botet R. *Aggregation and Fractal Aggregates*. World Scientific (1987).
648
- 649 28. Pérez-Alonso FJ, *et al.* Chemical Structures of Coprecipitated Fe–Ce Mixed Oxides. *Chem*
650 *Mater* **17**, 2329-2339 (2005).
651
- 652 29. Ball RC, Witten TA. Particle aggregation versus cluster aggregation in high dimensions. *J Stat*
653 *Phys* **36**, 873-879 (1984).
654
- 655 30. Poulin P, Bibette J, Weitz DA. From colloidal aggregation to spinodal decomposition in sticky
656 emulsions. *Eur Phys J B* **7**, 277-281 (1999).
657
- 658 31. Thouy R, Jullien R. A cluster-cluster aggregation model with tunable fractal dimension. *J Phys*
659 *A: Math Gen* **27**, 2953-2963 (1994).
660
- 661 32. Stanley HE. *Introduction to Phase Transitions and Critical Phenomena*. Oxford University Press
662 (1987).
663
- 664 33. Hunter RJ. *Foundations of Colloid Science*. Oxford University Press (2001).

- 665
666 34. Miller JT, Irish DE. Infrared and Raman spectra of the cerium(IV) ion – nitrate ion – water
667 system. *Can J Chem* **45**, 147-155 (1967).
668
- 669 35. Weber WH, Hass KC, McBride JR. Raman study of $\{\mathrm{CeO}\}_2$: Second-order
670 scattering, lattice dynamics, and particle-size effects. *Phys Rev B* **48**, 178-185 (1993).
671
- 672 36. Keramidas VG, White WB. Raman spectra of oxides with the fluorite structure. *J Chem Phys* **59**,
673 1561-1562 (1973).
674
- 675 37. Hassan MH, Andreescu D, Andreescu S. Cerium Oxide Nanoparticles Stabilized within Metal–
676 Organic Frameworks for the Degradation of Nerve Agents. *ACS Applied Nano Materials* **3**,
677 3288-3294 (2020).
678
- 679 38. Schilling C, Hofmann A, Hess C, Ganduglia-Pirovano MV. Raman Spectra of Polycrystalline
680 CeO₂: A Density Functional Theory Study. *J Phys Chem C* **121**, 20834-20849 (2017).
681
- 682 39. Chen S-Y, Chen R-J, Lee W, Dong C-L, Gloter A. Spectromicroscopic evidence of interstitial
683 and substitutional dopants in association with oxygen vacancies in Sm-doped ceria
684 nanoparticles. *Physical Chemistry Chemical Physics* **16**, 3274-3281 (2014).
685
- 686 40. Larsen RD, Brown GH. The Structure of Ammonium Hexanitratocerate(IV) in Solution I a. *J*
687 *Phys Chem* **68**, 3060-3062 (1964).
688
- 689 41. Briois V, *et al.* Time-Resolved Study of the Oxidation of Ethanol by Cerium(IV) Using
690 Combined Quick-XANES, UV–Vis, and Raman Spectroscopies. *J Phys Chem A* **109**, 320-329
691 (2005).
692
- 693 42. Nicolis G. *Self-organization in nonequilibrium systems : from dissipative structures to order*
694 *through fluctuations / G. Nicolis, I. Prigogine.* Wiley (1977).
695
- 696 43. Szabó Z, Toraishi T, Vallet V, Grenthe I. Solution coordination chemistry of actinides:
697 Thermodynamics, structure and reaction mechanisms. *Coord Chem Rev* **250**, 784-815 (2006).
698
- 699 44. Ginot F, Theurkauff I, Detcheverry F, Ybert C, Cottin-Bizonne C. Aggregation-fragmentation
700 and individual dynamics of active clusters. *Nat Commun* **9**, 696 (2018).
701
- 702 45. Strogatz SH. *Nonlinear dynamics and chaos : with applications to physics, biology, chemistry,*
703 *and engineering*, Second edition.. edn. Boulder, CO : Westview Press, a member of the Perseus
704 Books Group (2015).
705
- 706 46. Glansdorff P, Prigogine I. *Thermodynamic theory of structure, stability and fluctuations.* Wiley-
707 Interscience (1971).
708
- 709 47. Shi R, Tanaka H. Direct Evidence in the Scattering Function for the Coexistence of Two Types
710 of Local Structures in Liquid Water. *J Am Chem Soc* **142**, 2868-2875 (2020).
711
- 712 48. Servis MJ, Martinez-Baez E, Clark AE. Hierarchical phenomena in multicomponent liquids:
713 simulation methods, analysis, chemistry. *Phys Chem Chem Phys* **22**, 9850-9874 (2020).
714

- 715 49. Özkan E, *et al.* Peering into the Formation of Cerium Oxide Colloidal Particles in Solution by In
716 Situ Small-Angle X-ray Scattering. *Langmuir* **36**, 9175-9190 (2020).
717
- 718 50. Saeki M, *et al.* In Situ Time-Resolved XAFS Studies on Laser-Induced Particle Formation of
719 Palladium Metal in an Aqueous/EtOH Solution. *J Phys Chem C* **123**, 817-824 (2019).
720
- 721 51. Mu J, Motokawa R, Akutsu K, Nishitsuji S, Masters AJ. A Novel Microemulsion Phase
722 Transition: Toward the Elucidation of Third-Phase Formation in Spent Nuclear Fuel
723 Reprocessing. *J Phys Chem B* **122**, 1439-1452 (2018).
724
- 725 52. Orthaber D, Bergmann A, Glatter O. SAXS experiments on absolute scale with Kratky systems
726 using water as a secondary standard. *J Appl Crystallogr* **33**, 218-225 (2000).
727
- 728 53. Mu J, Motokawa R, Williams CD, Akutsu K, Nishitsuji S, Masters AJ. Comparative Molecular
729 Dynamics Study on Tri-n-butyl Phosphate in Organic and Aqueous Environments and Its
730 Relevance to Nuclear Extraction Processes. *J Phys Chem B* **120**, 5183-5193 (2016).
731
- 732 54. Pettersen EF, *et al.* UCSF Chimera—A visualization system for exploratory research and
733 analysis. *Journal of Computational Chemistry* **25**, 1605-1612 (2004).
734
- 735 55. Hunter JD. Matplotlib: A 2D Graphics Environment. *Computing in Science & Engineering* **9**, 90-
736 95 (2007).
737
- 738 56. Plakhova TV, *et al.* Solubility of Nanocrystalline Cerium Dioxide: Experimental Data and
739 Thermodynamic Modeling. *J Phys Chem C* **120**, 22615-22626 (2016).
740
- 741
- 742

743 **Acknowledgements**

744 This work was supported by the Japan Society for the Promotion of Science (JSPS) KAKENHI (Grant
745 Number JP20K05387) and Ministry of Education, Culture, Sports, Science and Technology (MEXT)
746 KAKENHI (Grant Numbers JP18KK0148 and JP18H01921). N. A. is grateful to the Advanced Science
747 Research Centre (ASRC), Japan Atomic Energy Agency (JAEA) for the REIMEI Research Fund 2021.

748 **Author Contributions**

749 N. A. designed the original project. N. A., R. M., and A. I.-O. guided the research. All authors interpreted
750 the results and contributed to the manuscript. N. A., S. N., and R. M. performed SAXS studies and R. M.
751 analysed the data. T. T. performed TEM. T. S. conducted zetasizer studies. T. Y. performed Raman
752 microscopy. N. A. prepared the samples. N. A. and M. O. performed theoretical modelling.

753
754 **Supplementary Information**

755 **Supplementary Information** accompanies this paper at <https://doi.org/10.XXX>

756
757 **Competing Interests**

758 The authors declare no competing financial interests.

759
760 **Materials & Correspondence**

761 **Corresponding Author**

762 *E-mail: aoyagi.noboru@jaea.go.jp. Tel: +81 29 284 3769.

763 **ORCID**

764 Aoyagi Noboru: 0000-0002-0913-2742

765

Supplementary Files

This is a list of supplementary files associated with this preprint. Click to download.

- [SupplementaryInformation.v1.pdf](#)